

Geophysical Research Letters[®]



RESEARCH LETTER

10.1029/2023GL106482

Key Points:

- Radiative cooling of the H₂O cloud influences the transport of the H₂O cloud, stratospheric dynamics and, changes tracer transport
- Radiative cooling of the H₂O cloud influences the cross equatorial transport of the H₂O cloud
- The phase of the QBO modulates the large-scale transport and the vertical extension of the HTHH cloud

Supporting Information:

Supporting Information may be found in the online version of this article.

Correspondence to:

U. Niemeier,
ulrike.niemeier@mpimet.mpg.de

Citation:

Niemeier, U., Wallis, S., Timmreck, C., van Pham, T., & von Savigny, C. (2023). How the Hunga Tonga—Hunga Ha'apai water vapor cloud impacts its transport through the stratosphere: Dynamical and radiative effects. *Geophysical Research Letters*, 50, e2023GL106482. <https://doi.org/10.1029/2023GL106482>

Received 19 SEP 2023

Accepted 2 DEC 2023

Author Contributions:

Conceptualization: Ulrike Niemeier

Formal analysis: Ulrike Niemeier, Sandra Wallis

Funding acquisition: Claudia Timmreck, Christian von Savigny

Project Administration: Christian von Savigny

Software: Ulrike Niemeier, Trang van Pham

Validation: Ulrike Niemeier, Sandra Wallis, Trang van Pham






Visualization: Ulrike Niemeier, Sandra Wallis

Writing – original draft: Ulrike Niemeier, Sandra Wallis

© 2023 The Authors.

This is an open access article under the terms of the [Creative Commons Attribution-NonCommercial License](https://creativecommons.org/licenses/by/4.0/), which permits use, distribution and reproduction in any medium, provided the original work is properly cited and is not used for commercial purposes.

How the Hunga Tonga—Hunga Ha'apai Water Vapor Cloud Impacts Its Transport Through the Stratosphere: Dynamical and Radiative Effects

Ulrike Niemeier¹ , Sandra Wallis² , Claudia Timmreck¹ , Trang van Pham³ , and Christian von Savigny² 

¹Max Planck Institute for Meteorology, Hamburg, Germany, ²Institute of Physics, University of Greifswald, Greifswald, Germany, ³German Weather Service, Offenbach, Germany

Abstract The eruption of the Hunga Tonga—Hunga Ha'apai (HTHH) volcano on 15 January 2022 injected about 150 Tg of water vapor (H₂O), roughly 10% of the background stratospheric H₂O content, to altitudes above 50 km. Simulations of the spatial evolution of the H₂O cloud with the ICON-Seamless model are very close to observations from the Aura Microwave Limb Sounder. The vertical transport of the H₂O cloud had three phases: an initial subsidence phase, a stable phase, and a rising phase. Radiative cooling of H₂O clearly affects the transport of the H₂O cloud, as demonstrated with passive tracers, and is the main driver within the subsidence phase. It also counteracts the large-scale rising motion in the tropics, leading to the stable phase, and modulates the large-scale transport of the H₂O cloud for about 9 months. This holds for different QBO phases, where the H₂O cloud differs mainly in its vertical extent.

Plain Language Summary The eruption of the Hunga Tonga—Hunga Ha'apai (HTHH) volcano on 15 January 2022 injected about 150 Tg water vapor (H₂O) to an altitude above 50 km. This is more than 10% of the total stratospheric H₂O content. We study the distribution of the H₂O cloud and its ascent into the mesosphere using observations from the Aura Microwave Limb Sounder satellite and by performing simulations of the cloud with the ICON-Seamless model. The vertical transport of the H₂O cloud had three phases: a subsidence, a stable, and a rising phase. The temperature inside the H₂O cloud is lower than outside the cloud. This causes the subsidence of the H₂O cloud and has consequences for the transport during the next months. From October 2022 on, the transport is mainly determined by the large-scale wind patterns.

1. Introduction

The stratosphere is a particularly dry atmospheric region. Water vapor enters the tropical stratosphere through the tropical tropopause layer, for example, by overshooting convection in the tropical tropopause region, and is subject to seasonal variations. The resulting distinct patterns of water vapor in the tropical stratosphere are called tape recorder effect (Mote et al., 1996). The Hunga Tonga—Hunga Ha'apai (HTHH) eruption on 15 January 2022 (20.54°S and 175.38°W) disrupts the regular tape recorder pattern by emitting 146 ± 5 Tg H₂O of water vapor (e.g., Khaykin et al., 2022; Millán et al., 2022), and additionally 0.4–0.5 Tg sulfur dioxide (SO₂) (Carr et al., 2022). The volcanic vent was submerged about 150 m below the water surface during the eruption, a consequence of the extreme explosion, probably caused by the contact of magma and water, which transported the volcanic cloud up to 55 km (Carr et al., 2022) or even 57 km altitude (Proud et al., 2022).

Several papers describe the H₂O cloud after the HTHH eruption during the first days and months, for example, Millán et al. (2022), Vömel et al. (2022), Schoeberl et al. (2022, 2023), and Zhu et al. (2022). The cloud showed a rapid descent from the initial injection height of about 50 km (1 hPa) to an altitude range of 22–27 km (40–20 hPa) in the first weeks after the eruption in the latitudinal range between 10° and 20°S (Figure 1a). Several theories have been proposed to explain this descent. Schoeberl et al. (2022) suggested that volcanic water vapor immediately formed ice particles that sedimented. Legras et al. (2022), however, proposed that the descent was caused by radiative cooling due to infrared emission by water vapor. This process appears to be relevant to downwelling as long as the H₂O cloud is sufficiently concentrated (Sellitto et al., 2022). After this rapid descent, the cloud remains at the same altitude for several months, which is distinctly different from the tape recorder effect, before it begins to rise. Another peculiarity is the cross-equatorial transport of the H₂O cloud during this phase as discussed by Schoeberl et al. (2023).

Writing – review & editing: Claudia Timmreck, Trang van Pham, Christian von Savigny

In this paper, we seek to understand the role of radiative cooling of the H₂O cloud on the large-scale transport in the stratosphere and the extent to which the transport is influenced by other factors, such as the Quasi-Biennial Oscillation (QBO) and the Brewer-Dobson Circulation (BDC). Therefore, we study the spatial evolution of the volcanic H₂O cloud over a period of about one and a half years in two ways: We analyze H₂O mixing ratio observations provided by the Microwave Limb Sounder (MLS) instrument onboard the Aura satellite and simulate the transport of the HTHH H₂O cloud using the ICON-Seamless model including passive tracers.

This paper is structured as follows. Section 2 gives a brief description of the MLS instrument, the analysis of the MLS data, and of the ICON-Seamless model. Section 3 presents the transport pattern of the H₂O cloud as a comparison between observational and model results. The role of the radiative interaction of the H₂O cloud is discussed in Section 4, followed by a conclusion in Section 5.

2. Methodology

2.1. Observations

We use NASA MLS level 2 version 5 H₂O mixing ratios to follow the transport of the HTHH H₂O cloud. The Earth Observing System Microwave Limb Sounder was launched onboard the Aura satellite (Waters et al., 2006). It is a limb sounding instrument measuring in the microwave spectral region using frequencies at 118, 190, 240, and 640 GHz and 2.5 THz. The Aura satellite has a sun-synchronous, near-polar orbit with an inclination of 98°, allowing MLS measurements from 82°N to 82°S.

The vertical resolution of the H₂O data product varies with pressure level and is approximately 1.3–3.6 km between 316 and 0.22 hPa and 6–11 km above 0.22 hPa (Livesey et al., 2022). Only mixing ratios between 316 and 0.001 hPa are recommended for scientific use. The precision is 5%–16% and the accuracy is 5%–35% between 316 and 1 hPa. The measurements were filtered according to the MLS Aura document (Livesey et al., 2022), that is, positive estimated precision, status field an even number, quality greater than 0.7, and convergence less than 2.0. Additionally, profiles with H₂O mixing ratios <0.101 ppmv at altitudes ≤1 hPa were dismissed. H₂O anomaly time series were determined by subtracting multi-year daily average MLS H₂O mixing ratios from the 5-year period between 2017 and 2021. Only H₂O anomalies larger than 5 times the standard deviation of the reference period are considered significant. We use this high value to emphasize the strong HTHH signal. The stratopause was determined as the temperature maximum from vertically smoothed MLS temperature profiles using a 2.6 km boxcar average.

2.2. Model Description and Simulations

Within this study we use a coarse resolution version of the numerical weather prediction (NWP) configuration of the ICON atmosphere model (Zängl et al., 2015), the ICON-Seamless model (Früh et al., 2022), where the land model and the vertical diffusion scheme of the NWP configuration are replaced by the JSBACH model (Reick et al., 2021). ICON uses a triangular grid which is derived from a spherical icosahedron by repeated subdivision of the spherical triangular cells into smaller cells (Wan et al., 2013). The model equations are integrated over time in the dynamical core, with a time step of 360 s. Further detailed descriptions of ICON-NWP can be found in Zängl et al. (2015) and Rieger et al. (2015).

The horizontal resolution of the model is R2B4, corresponding to about 160 km. The model has 130 vertical levels with a maximum vertical grid spacing of 500 m up to 35 km, which is then increasing to 1,400 m up to the model top at 75 km. This allows internal generation of the quasi-biennial oscillation (QBO). Sea surface temperatures (SSTs) are prescribed (see Giorgetta et al. (2018) for details) based on the Atmospheric Model Intercomparison Project SST observational data set (Hurrell et al., 2008). For tropospheric aerosols, the annually repeating monthly mean climatology from the Max Planck Institute Aerosol Climatology (MAC; Kinne et al., 2013) is used.

The simulations of the two QBO phases were initialized with European Centre for Medium-Range Weather Forecasts reanalysis (ERA5) data (Hersbach et al., 2020) for 15 January 2022 with an easterly jet (HTHH_E), and 15 January 1988, with a westerly jet around 25 hPa (Table 1). This model state is integrated in time without further reference to observations, except for transient boundary conditions. To simulate the estimated water vapor injection, we changed the temperature and specific humidity in the ERA5 initial data corresponding to the HTHH

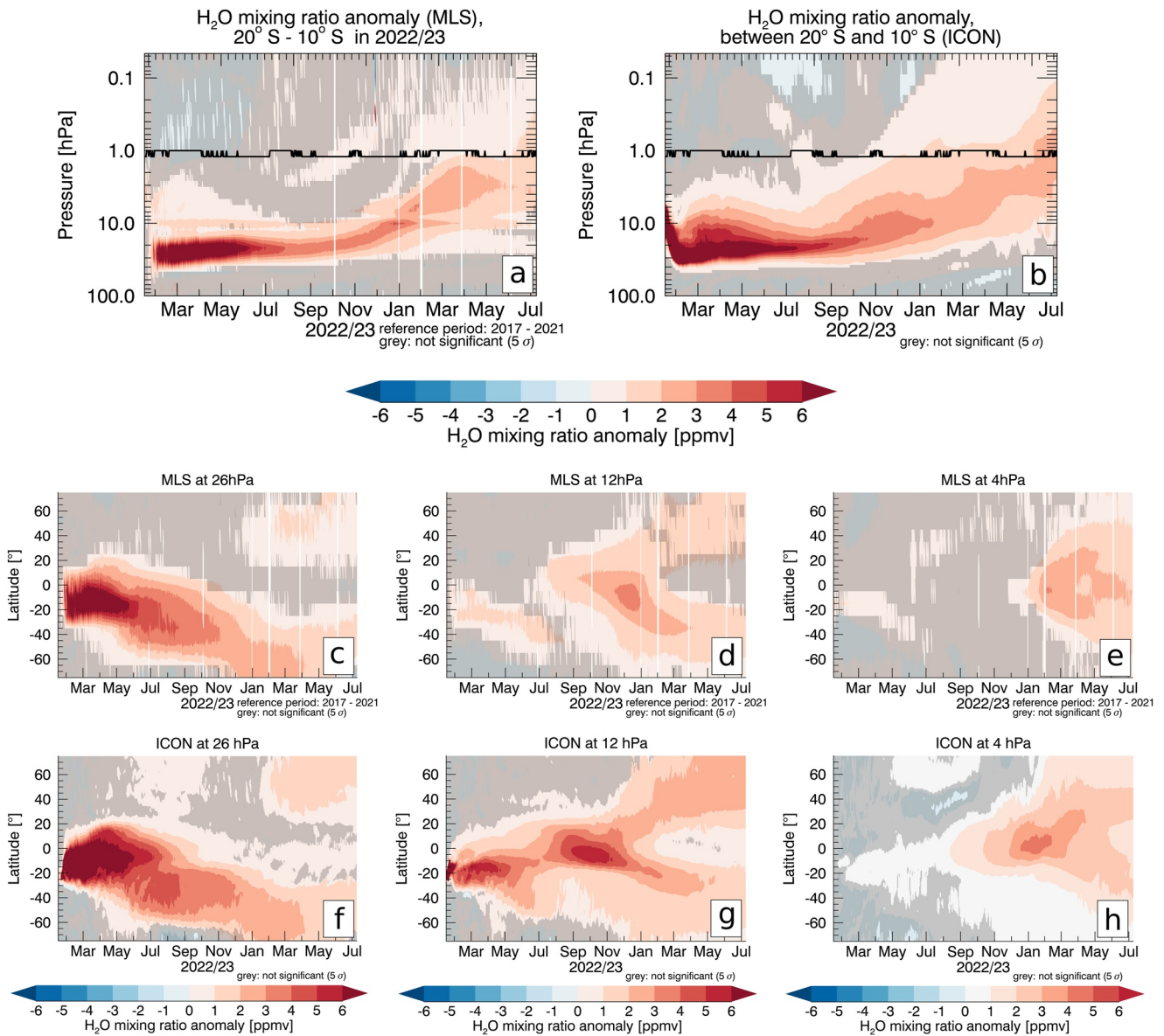


Figure 1. Hovmöller plots of vertical and horizontal transport of the H₂O cloud. Top (a and b): Vertical cross section of daily averages of zonal and latitudinal (10°–20°S) mean water vapor anomalies from (a) MLS observations and (b) simulation results of ICON-Seamless (HTHH_E). The stratopause (black line) in both plots was estimated from the MLS temperature observations. Bottom (c–h): MLS H₂O anomalies at the pressure levels (c) 26 hPa, (d) 12 hPa and (e) 4 hPa and (f–h) simulated H₂O anomalies at similar pressure levels. H₂O anomalies that are not significant at the 5σ-level of the reference H₂O mixing ratios are shaded in gray.

Table 1

Overview of the Performed Model Simulations Including Information on the Injection of Water Vapor, the Passive Tracers and the QBO Phase

Experiment	Tracer	Initialization	QBO phase
HTHH_E	H ₂ O	15 January 2022 full initial state of ERA 5	East at 40–20 hPa in January 2022
CTRL_E	None	HTHH_E	HTHH_E
HTHH_W	H ₂ O	15 January 1988 with full initial state of ERA 5	West at 40–20 hPa in January 1988
CTRL_W	None	HTHH_W	HTHH_W
Pt_Jan	Passive	January 15 at 39 grid points with water vapor concentration >72 ppmv	
Pt_Feb	Passive	February 1 at 2,697 grid points with water vapor concentration >48 ppmv	

location: 150 Tg of H₂O were distributed over three horizontal grid points between altitudes of 40 and 45.5 km, and the temperature was set to 244 K similar to Millán et al. (2022). We do not consider other volcanic emissions, such as sulfur and ash, and associated ozone anomalies.

Passive tracers were injected into the stratosphere on two different dates to separately cover two phases of H₂O cloud behavior, the initial descent and the subsequent transport. To match the HTHH H₂O cloud patterns the passive tracer concentrations were set to 1 kg/kg at grid points where the water vapor mixing ratio is above a certain threshold. Consequently, the injected tracer masses for the differ (Table 1) and the passive tracers have been scaled by the injected mass in the analysis, resulting in unitless values. All anomalies are calculated as differences from the corresponding control simulations.

3. Results

The water vapor injected by the eruption of the HTHH volcano on 15 January 2022 is distributed throughout the stratosphere. Figure 1a shows the observed evolution of the mean vertical distribution of the H₂O cloud from 15 January 2022 to 9 July 2023 in the tropical region between 10°S and 20°S. The anomaly is detected up to nearly 1 hPa immediately after the volcanic eruption, and descends rapidly to 40–20 hPa altitude by the end of January. The H₂O cloud remains at these altitudes until October 2022 and then begins to rise, reaching altitudes up to 1 hPa (the stratopause region) by the end of March 2023. The apparently low H₂O anomaly during the first weeks after the eruption is a result of the data filtering criteria used in this study (see Section 2.1). Immediately after the HTHH eruption, some H₂O profiles do not pass the filtering criteria recommended in Livesey et al. (2022), due to the large amount of H₂O and the unusually high injection. Retrieval performance returned to normal by 8 February 2022 (Millán et al., 2022). There is an artifact at 10 hPa that seemed to be caused by the placement of the MLS spectral channels around the water vapor line.

The simulated H₂O cloud (Figure 1b) mirrors the observations in many aspects. The cloud subsides to similar levels in the 40–20 hPa range and begins to rise again in October 2022. The vertical extension of the cloud is slightly different, especially the first upwelling of parts of the cloud in March and April 2022. As a result, when the cloud begins to rise in October 2022, the vertical extent is greater in the model and the 1 hPa level is reached 2 months earlier in the model than in the MLS data.

The main part of the observed H₂O cloud between 40 and 20 hPa was confined between 20°N and 30°S until May 2022, when parts of the cloud started to disperse toward the southern polar region (Figure 1c). At 26 hPa, the cloud reached 50 to 60°S in June, when the Southern Hemispheric (SH) polar vortex blocked further southward transport. The vortex broke up in October, and the cloud reached the SH pole in December 2022. At 12 hPa (Figure 1d), the H₂O mixing ratio increased between 20°N and 0° around mid-July 2022, shortly after the cloud began to rise. In February 2023, this anomaly splits into a northward and a southward branch. Finally, the cloud reaches 4 hPa in the tropics in January 2023, where it also begins to spread toward the mid-latitudes of both hemispheres (Figure 1e).

At an altitude of 26 hPa, the meridional transport of the simulated H₂O cloud was blocked by the subtropical transport barrier and the polar vortex (Figure 1f) similar to the measurements (Figure 1c). The vortex broke up slightly later than observed. Part of the cloud appeared at high northern latitudes in early 2023 in both observations and simulations. The water vapor reached these levels by descending air masses from the upper branch of the BDC. At 12 hPa the simulated water vapor cloud (Figure 1g) has slightly higher mixing ratios than in the observations (Figure 1d) as a consequence of the earlier upwelling in March. Also, the equatorial crossing of the bulk of the H₂O cloud occurs earlier, in August instead of September. The splitting of the cloud into a northern and a southern branch is simulated very well. Observations and simulations are similar at 4 hPa, although with higher concentrations in the simulations and the earlier appearance of the simulated anomalies, as at the level below (Figure 1h).

In the following, we discuss the implications of the cooling within the H₂O cloud and the QBO on the transport of the H₂O cloud by using passive tracers. They follow the vertical distribution of the H₂O cloud in the inner tropics very well in both simulated QBO phases (Figures 2a and 2g). Averages over 10°–20°S are shown in Supporting Information S1 (Figure S1).

4. Discussion

The vertical transport of the H₂O cloud can be separated into three phases (Figure 1a): The initial subsidence phase during the first 2 weeks, a stable phase where the cloud remains at similar altitudes until October 2022 and

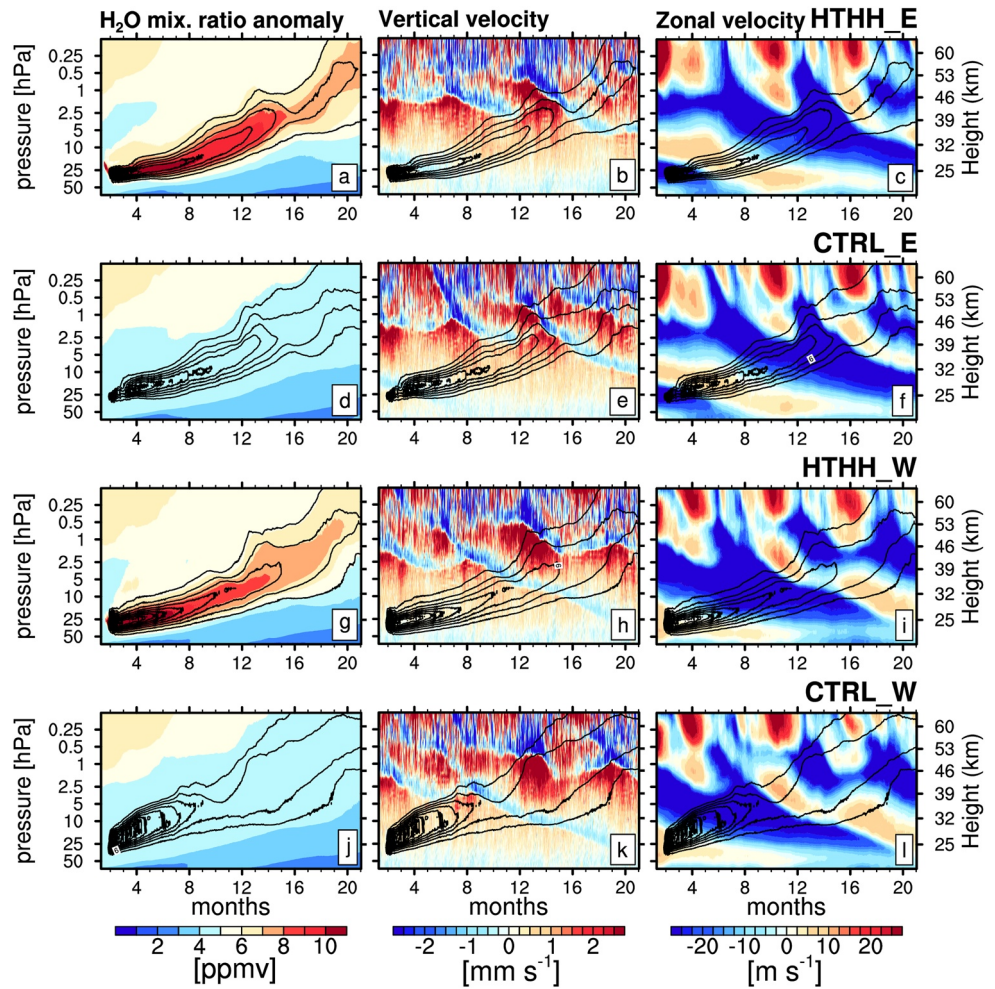


Figure 2. Hovmöller plots of vertical profiles of zonally averaged water vapor anomaly (left), vertical velocity (middle), and zonal wind (right), averaged over the inner tropics (5°N and 5°S). The rows show the results of different model simulations: (a–c) starting on the HTHH eruption day (HTHH_E) with an easterly QBO phase, (g–i) starting in an easterly QBO phase (HTHH_W), and the two corresponding control simulations without HTHH eruption (d–f and j–l). The contours show the distribution of passive tracers starting on February 1. Values averaged between 10 and 20°S are given in Supporting Information S1 (Figure S1).

the following rising phase. The first two phases differ from the normal behavior of water vapor in the stratosphere which is characterized by the tape recorder effect. This is illustrated by passive tracers (Figure 3a). Injecting the tracers right after the eruption (PtJan) shows for HTHH_E the subsidence of the tracers during the first 2 weeks, in contrast to CTRL_E where the tracers rise rapidly to altitudes above 10 hPa.

Water vapor interferes with solar and terrestrial radiation. This leads to cooling anomalies within the H_2O cloud of -7 to -1 K/day during the first 2 weeks (Figure 3e) and a negative temperature anomaly of up to -4 K for several months (Figure 3d). This corresponds to negative vertical velocity anomalies for most of the H_2O cloud (Figure 3f), an absolute downdraft velocity of up to -12 mm/s (about 1 km/day) on the first day (Figure 3g), and up to -3 mm/s (260 m/day) in the following days after the eruption, decreasing to -1 mm/s (86 m/day) at the end of January. Our simulated vertical velocities are very similar to those calculated by Randel et al. (2023), using COSMIC-2 GNSS radio occultation data. From February on, the vertical velocity anomalies and absolute values become smaller (Figures 3f and 3g), but remain mostly negative until March, in agreement with the estimates of Legras et al. (2022) where the vertical velocity from MLS data became positive in mid-February. The subsidence phase ends in early February as the radiative cooling diminishes (Figure 3e), but the ongoing cooling of the H_2O cloud and the related subsidence motion prevent the H_2O cloud from rising in the tropical stratosphere as in unperturbed conditions, resulting in a stable phase until autumn 2022. The passive tracers illustrate the impact of

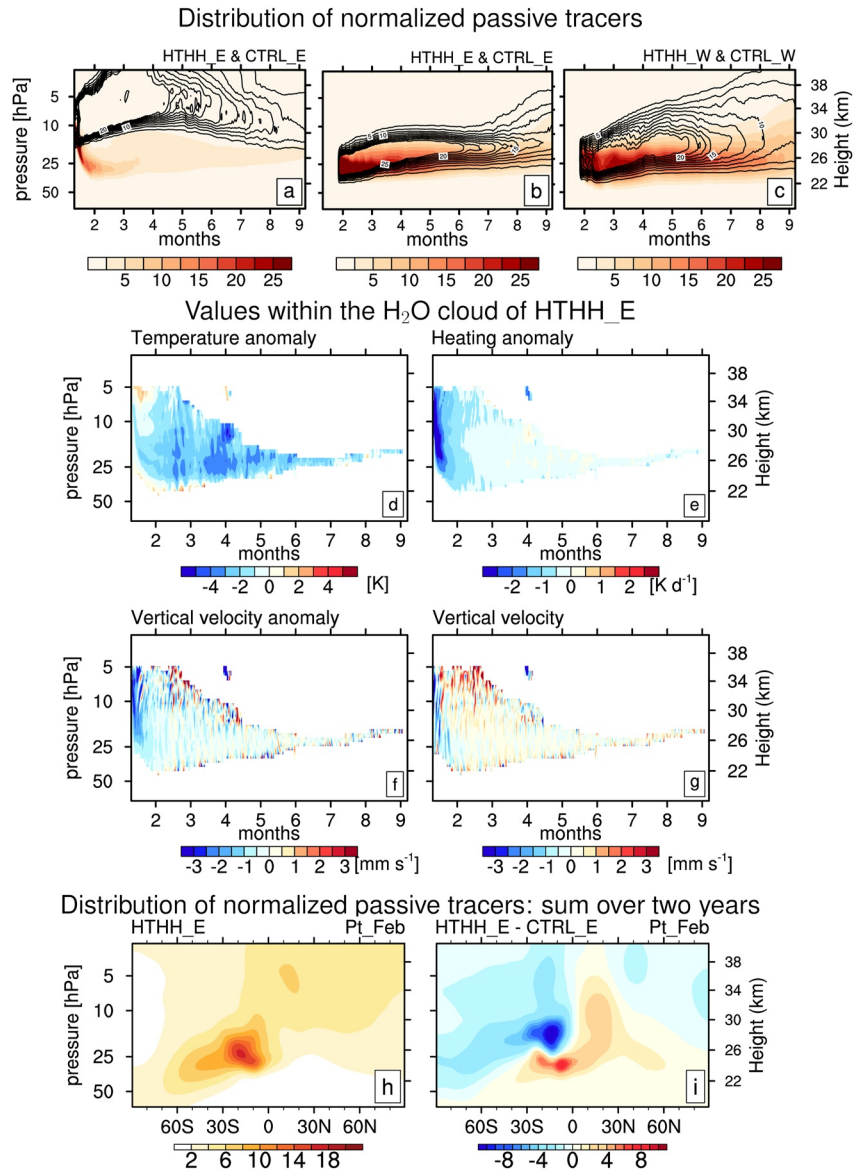


Figure 3. Top: Hovmöller plots of the normalized passive tracer distribution for a simulation with (shaded) and without HTHH H₂O injection (contours) averaged between 10 and 20°S. The passive tracers are initialized on (a) January 15 (Pt_Jan) and (b) February 1 (Pt_Feb). (c) Same as (b), but for a QBO westerly phase. Middle: Hovmöller plots of daily mean anomalies within the H₂O cloud of (d) temperature, (e) radiative heating rate, (f) vertical velocity, and (g) absolute values of vertical velocity. The averages include all grid points within the H₂O cloud where the water vapor mixing ratio is greater than 12 ppmv. Bottom: Distribution of zonally averaged passive tracers of (h) HTHH_E and (i) the anomaly to CTRL_E. Monthly mean data were integrated over 2 years to obtain the distribution shown.

radiative cooling on the transport processes. Injected into the lower part of the H₂O cloud (PtFeb), they behave similarly to the volcanic H₂O cloud in HTHH_E while rising immediately after injection in CTRL_E (Figure 3b).

The QBO impacts the transport of the volcanic H₂O cloud mainly in the stable phase (Figure 2). Until May, the H₂O cloud at 26 hPa is confined between 20°N and 30°S (Figure 1c). Poleward transport is blocked in the summer hemisphere by a subtropical transport barrier at about 20° (Punge et al., 2009), which prevents transport of the bulk of the H₂O cloud into the SH extra-tropics until May. However, the extension of the H₂O cloud to 20°N is unusual (Figures 1c and 1f). The position of the H₂O cloud coincides with an easterly jet of the QBO (Figure 2c) where planetary waves cannot enter the easterly jet. This should prevent the H₂O cloud from crossing the equator. Schoeberl et al. (2023) highlight this equatorial crossing to 20°N in April–July and point to the

descending westerly wind regime as the cause. According to our passive tracer simulations, the equatorial crossing is enhanced by the radiative cooling of the H₂O cloud (Figures S2a and S2d in Supporting Information S1) and does not occur in the simulations with a different QBO phase (Figures S2g and S2j in Supporting Information S1). While the meridional transport of the passive tracers of PtFeb differs in detail between HTHH_E and HTHH_W, the overall picture is similar and more dominated by the BDC than by the QBO phases, for example, in May the H₂O cloud can cross the subtropical transport barrier in both QBO phases.

The vertical transport is quite similar between the two simulated QBO phases. Both show the stable phase (Figure 2). The radiative cooling impact keeps the H₂O cloud at a similar altitude until October. However, according to Schoeberl et al. (2023), the upwelling in March 2023 (Figures 1a and 1b) can be related to the QBO phase. In addition, the stable phase of HTHH_E coincides with a transition to westerly jets at 26 hPa, and negative vertical velocities in the easterly shear zone above prevent the cloud from rising further (Figure 2b). In HTHH_W the passive tracers rise more than in HTHH_E and even more in CTRL_W (Figures 2g–2l and 3c). Thus, in HTHH_E, the stable phase is caused by radiative cooling plus the QBO phase is associated with negative vertical velocities, while in HTHH_W only radiative cooling is the cause, since the zonally averaged vertical velocities are positive (Figure 2h). As the cooling impact diminishes in September, the rising phase of the cloud begins (Figure 3d), and the tracers follow the advection described by the zonal winds and the associated vertical velocity (Figures 3c and 3i).

The zonal wind anomaly of the HTHH simulations against the corresponding control simulations (Figure S3 in Supporting Information S1) shows reduced zonal wind velocities for both QBO phases within the H₂O cloud. This leads to an increase in the easterly components of the zonal winds within the H₂O cloud, while the westerly component increases around the cloud, for example, the tail of the zonal wind at 50 hPa (Figures 2c and 2f). This behavior is consistent with previous model results on the influence of stratospheric sulfur on zonal winds (Aquila et al., 2014; Niemeier & Schmidt, 2017), but is difficult to detect from observations. One consequence is enhanced transport across the equator (Schoeberl et al., 2023). The longer term effect on transport is shown by the time integral of the passive tracers (Figure 3h) and the difference to CTRL_E (Figure 3i). The maximum around 15°S is at lower altitudes, meridional transport to the SH mid-latitudes is reduced and shifted to lower altitudes, and transport to the Northern Hemisphere (NH) is increased. This is consistent with the observed pattern of ozone anomalies after the HTHH eruption (Basha et al., 2023): In the tropics, the observed ozone anomaly is positive between 20 and 50 hPa and negative above that. The observed ozone anomalies in the SH are also negative in the lower stratosphere, implying reduced transport, in the second half of 2022, but positive in the NH. This may indicate an impact of changing transport patterns on ozone, as the passive tracers indicated in our simulations. Our study does not include ozone chemistry, so further analysis is beyond the scope of this paper.

Thus, the role of the radiative impact of the H₂O cloud is particularly important in the first months after the eruption. The results on the vertical velocity in the H₂O cloud and the temperature anomaly (Figure 3e), together with the behavior of the passive tracers, show that the main reason for the subsidence of the H₂O cloud must be the strong radiative cooling of the water vapor. Ice particles sediment and would leave no trace in either the vertical velocity or the advective tracer transport. According to simulations, ice particles are only a small fraction of the H₂O cloud. Zhu et al. (2022) simulated about 10% ice in the first 2 days and our simulations show much less ice.

5. Summary and Conclusion

In January 2022, Hunga Tonga—Hunga Ha'apai emitted about 150 Tg H₂O into the tropical middle atmosphere. The H₂O cloud descended rapidly over the next 2 weeks and remained at altitudes between 40 and 20 hPa between 10°S and 20°S. We tracked the H₂O cloud with MLS satellite observations until July 2023 and compared the transport of the H₂O cloud between MLS and model simulations, performed with the new ICON-Seamless model. We defined three phases for the evolution of the H₂O cloud: a subsidence, a stable, and a rising phase. Our analysis showed that the radiative cooling of the H₂O is the main driver within the subsidence phase. During all months of the stable phase the radiative cooling continues to affect the vertical velocities and the cloud rises less than in the control simulations without the HTHH eruption. Temperature anomalies and vertical velocities within the H₂O cloud differ from the zonal averages outside the cloud during this period. Vertical velocities associated with the easterly QBO phase enhance the radiative effects. Thereafter the transport is dominated by the large-scale wind patterns.

The passive tracer studies allowed us to determine the radiative forcing impact of water vapor on the transport. We found in simulation HTHH_E reduced vertical transport in the tropics, reduced meridional transport into the southern hemisphere and a slightly increased transport into the northern hemisphere. This compares well with observed ozone anomalies (Basha et al., 2023). However, we have not included sulfate aerosols or ash injected by the HTHH eruption, nor the impact of ozone anomalies caused by the eruption. These species also interact with radiation and add warming (ash, sulfate) or further cooling in the case of a negative ozone anomaly. Therefore, our tracers indicate changes in transport caused solely by the water vapor anomalies. Overall, the spatial and temporal distributions of the simulated H₂O cloud are very close to the MLS observations. There are small differences in the timing and vertical position of the simulated H₂O cloud, but they are close to the observations for a free-running model. We conclude from these similarities that the heating anomalies of sulfur, ash and changes in the ozone concentrations are less important for the transport of the H₂O cloud than the heating anomalies of the water vapor.

The comparison to MLS data and the detailed analysis of the transport during the first months after the eruption shows the importance of realistically simulated stratospheric dynamical conditions, in particular realistic phases of the QBO, which clearly influence the transport. If these conditions are not fulfilled, the simulated vertical velocities would not be comparable to the observations.

Conflict of Interest

The authors declare no conflicts of interest relevant to this study.

Data Availability Statement

MLS level 2 version 5 H₂O mixing ratios were provided from the NASA GES DISC website (Lambert et al., 2020). Simulation results described in this article are available in Niemeier (2023). Information on the model code are described in Supporting Information S1.

Acknowledgments

We thank Daniele Visione for the helpful suggestions as reviewer, colleagues at the German Weather Service and MPI for Meteorology for fruitful and helpful discussion, Daniel Reinert, Günther Zängl, Martin Köhler, Marco Giorgetta, Luis Kornblüeh, Andrea Schneidereit, as well as Yaga Richter (NCAR) for discussions on tuning the stratosphere. This study is part of the research unit FOR 2820 VollImpact (Grant 398006378) and funded by the German Research Foundation (DFG) within the projects VOLARC (UN, CvS), VolDyn (SW), and VolClim (CT). ICON-Seamless development of TvP was carried out in the project “Tuning von ICON-NWV und ICON-Seamless für Klimavorhersagen” (IAFE VH 3.4—TUCCO-O) within the Innovation Programme for applied researches and Developments (IAFE) from Deutscher Wetterdienst. The authors are indebted to the MLS team for providing and maintaining the high quality MLS/Aura data products. Computations and analysis were performed on the computer of the Deutsches Klima Rechenzentrum (DKRZ) using resources granted by its Scientific Steering Committee (WLA) under project ID bb1093. Open Access funding enabled and organized by Projekt DEAL.

References

- Aquila, V., Garfinkel, C. I., Newman, P., Oman, L., & Waugh, D. (2014). Modifications of the quasi-biennial oscillation by a geoengineering perturbation of the stratospheric aerosol layer. *Geophysical Research Letters*, *41*(5), 1738–1744. <https://doi.org/10.1002/2013GL058818>
- Basha, G., Ratnam, M. V., Kumar, A. H., Jiang, J. H., Babu, S. R., & Kishore, P. (2023). Impact of Hunga Tonga-Hunga Ha’apai volcanic eruption on stratospheric water vapour, temperature, and ozone. *Remote Sensing*, *15*(14), 3602. <https://doi.org/10.3390/rs15143602>
- Carn, S., Krotkov, N., Fisher, B., & Li, C. (2022). Out of the blue: Volcanic SO₂ emissions during the 2021–2022 eruptions of Hunga Tonga—Hunga Ha’apai (Tonga). *Frontiers in Earth Science*, *10*, 976962. <https://doi.org/10.3389/feart.2022.976962>
- Carr, J. L., Horváth, A., Wu, D. L., & Friberg, M. D. (2022). Stereo plume height and motion retrievals for the record-setting Hunga Tonga-Hunga Ha’apai eruption of 15 January 2022. *Geophysical Research Letters*, *49*(9), e2022GL098131. <https://doi.org/10.1029/2022GL098131>
- Früh, B., Potthast, R., Müller, W., Korn, P., Brienen, S., Fröhlich, K., et al. (2022). ICON-seamless, the development of a novel Earth System Model based on ICON for time scales from weather to climate. <https://doi.org/10.5194/ems2022-292>
- Giorgetta, M. A., Brokopf, R., Crueger, T., Esch, M., Fiedler, S., Helmert, J., et al. (2018). ICON-A, the atmosphere component of the ICON Earth system model: I. Model description. *Journal of Advances in Modeling Earth Systems*, *10*(7), 1613–1637. <https://doi.org/10.1029/2017ms001242>
- Hersbach, H., Bell, B., Berrisford, P., Hirahara, S., Horányi, A., Muñoz-Sabater, J., et al. (2020). The ERA5 global reanalysis. *Quarterly Journal of the Royal Meteorological Society*, *146*(730), 1999–2049. <https://doi.org/10.1002/qj.3803>
- Hurrell, J. W., Hack, J. J., Shea, D., Caron, J. M., & Rosinski, J. (2008). A new sea surface temperature and sea ice boundary dataset for the community atmosphere model. *Journal of Climate*, *21*(19), 5145–5153. <https://doi.org/10.1175/2008jcli2292.1>
- Khaykin, S., Podglajen, A., Ploeger, F., Grooß, J.-U., Tencé, F., Bekki, S., et al. (2022). Global perturbation of stratospheric water and aerosol burden by Hunga eruption. *Communications Earth & Environment*, *3*(1), 316. <https://doi.org/10.1038/s43247-022-00652-x>
- Kinne, S., O’Donnell, D., Stier, P., Kloster, S., Zhang, K., Schmidt, H., et al. (2013). MAC-v1: A new global aerosol climatology for climate studies. *Journal of Advances in Modeling Earth Systems*, *5*(4), 704–740. <https://doi.org/10.1002/jame.20035>
- Lambert, A., Read, W., & Livesey, N. (2020). *MLS/Aura level 2 water vapor (H₂O) mixing ratio V005*. Goddard Earth Sciences Data and Information Services Center (GES DISC). <https://doi.org/10.5067/Aura/MLS/DATA2508>
- Legras, B., Duchamp, C., Sellitto, P., Podglajen, A., Carboni, E., Siddans, R., et al. (2022). The evolution and dynamics of the Hunga Tonga plume in the stratosphere. *EGU Sphere*, *1–19*. <https://doi.org/10.5194/egusphere-2022-517>
- Livesey, N. J., Read, W. G., Wagner, P. A., Froidevaux, L., Santee, M. L., Schwartz, M. J., et al. (2022). Earth observing system (EOS) aura microwave limb sounder (MLS) version 5.0x level 2 and 3 data quality and description document. JPL D-105336 Rev. B, 5.0—1.1 a. Retrieved from https://mls.jpl.nasa.gov/data/v5-0_data_quality_document.pdf
- Millán, L., Santee, M. L., Lambert, A., Livesey, N. J., Werner, F., Schwartz, M. J., et al. (2022). The Hunga Tonga-Hunga Ha’apai hydration of the stratosphere. *Geophysical Research Letters*, *49*(13), e2022GL099381. <https://doi.org/10.1029/2022GL099381>
- Mote, P. W., Rosenlof, K. H., McIntyre, M. E., Carr, E. S., Gille, J. C., Holton, J. R., et al. (1996). An atmospheric tape recorder: The imprint of tropical tropopause temperatures on stratospheric water vapor. *Journal of Geophysical Research*, *101*(D2), 3989–4006. <https://doi.org/10.1029/95JD03422>

- Niemeier, U. (2023). *Data provided for Niemeier et al (2023): Hunga Tonga—Hunga Ha'apai water vapor plume: How the plume impacts its transport through the stratosphere through dynamical and radiative effects*. DOKU at DKRZ. Retrieved from <https://hdl.handle.net/21.14106/a78ab16a5ca2f2446938a112c8f5b43f8719379d>
- Niemeier, U., & Schmidt, H. (2017). Changing transport processes in the stratosphere by radiative heating of sulfate aerosols. *Atmospheric Chemistry and Physics*, 17(24), 14871–14886. <https://doi.org/10.5194/acp-17-14871-2017>
- Proud, S. R., Prata, A. T., & Schmauß, S. (2022). The January 2022 eruption of Hunga Tonga-Hunga Ha'apai volcano reached the mesosphere. *Science*, 378(6619), 554–557. <https://doi.org/10.1126/science.abo4076>
- Punge, H. J., Konopka, P., Giorgetta, M. A., & Müller, R. (2009). Effects of the quasi-biennial oscillation on low-latitude transport in the stratosphere derived from trajectory calculations. *Journal of Geophysical Research*, 114(D3), D03102. <https://doi.org/10.1029/2008JD010518>
- Randel, W. J., Johnston, B. R., Braun, J. J., Sokolovskiy, S., Vömel, H., Podglajen, A., & Legras, B. (2023). Stratospheric water vapor from the Hunga Tonga Hunga Ha'apai volcanic eruption deduced from COSMIC-2 radio occultation. *Remote Sensing*, 15(8), 2167. <https://doi.org/10.3390/rs15082167>
- Reick, C. H., Gayler, V., Goll, D., Hagemann, S., Heidkamp, M., Nabel, J. E. M. S., et al. (2021). JSBACH 3- The land component of the MPI Earth System Model: Documentation of version 3.2. *Berichte zur Erdsystemforschung*, 240. <https://doi.org/10.17617/2.3279802>
- Rieger, D., Bangert, M., Bischoff-Gauss, I., Förstner, J., Lundgren, K., Reinert, D., et al. (2015). ICON-ART 1.0—A new online-coupled model system from the global to regional scale. *Geoscientific Model Development*, 8(6), 1659–1676. <https://doi.org/10.5194/gmd-8-1659-2015>
- Schoeberl, M. R., Wang, Y., Ueyama, R., Taha, G., Jensen, E., & Yu, W. (2022). Analysis and impact of the Hunga Tonga-Hunga Ha'apai stratospheric water vapor plume. *Geophysical Research Letters*, 49(20), e2022GL100248. <https://doi.org/10.1029/2022GL100248>
- Schoeberl, M. R., Wang, Y., Ueyama, R., Taha, G., & Yu, W. (2023). The cross equatorial transport of the Hunga Tonga-Hunga Ha'apai eruption plume. *Geophysical Research Letters*, 50(4), e2022GL102443. <https://doi.org/10.1029/2022GL102443>
- Sellitto, P., Podglajen, A., Belhadji, R., Boichu, M., Carboni, E., Cuesta, J., et al. (2022). The unexpected radiative impact of the Hunga Tonga eruption of 15th January 2022. *Communications Earth and Environment*, 3(1), 288. <https://doi.org/10.1038/s43247-022-00618-z>
- Vömel, H., Evan, S., & Tully, M. (2022). Water vapor injection into the stratosphere by Hunga Tonga-Hunga Ha'apai. *Science*, 377(6613), 1444–1447. <https://doi.org/10.1126/science.abq2299>
- Wan, H., Giorgetta, M. A., Zängl, G., Restelli, M., Majewski, D., Bonaventura, L., et al. (2013). The ICON-1.2 hydrostatic atmospheric dynamical core on triangular grids—Part 1: Formulation and performance of the baseline version. *Geoscientific Model Development*, 6(3), 735–763. <https://doi.org/10.5194/gmd-6-735-2013>
- Waters, J., Froidevaux, L., Harwood, R., Jarnot, R., Pickett, H., Read, W., et al. (2006). The Earth observing system microwave limb sounder (EOS MLS) on the aura satellite. *Geoscience and Remote Sensing*, 44(5), 1075–1092. <https://doi.org/10.1109/TGRS.2006.873771>
- Zängl, G., Reinert, D., Rípodas, P., & Baldauf, M. (2015). The ICON (ICOSahedral non-hydrostatic) modelling framework of DWD and MPI-M: Description of the non-hydrostatic dynamical core. *Quarterly Journal of the Royal Meteorological Society*, 141(687), 563–579. <https://doi.org/10.1002/qj.2378>
- Zhu, Y., Bardeen, C. G., Tilmes, S., Mills, M. J., Wang, X., Harvey, V. L., et al. (2022). Perturbations in stratospheric aerosol evolution due to the water-rich plume of the 2022 Hunga-Tonga eruption. *Communications Earth and Environment*, 3(1), 248. <https://doi.org/10.1038/s43247-022-00580-w>